An adaptive feedback circuit for MEMS resonators

2011 J. Micromech. Microeng. 21 045008

(http://iopscience.iop.org/0960-1317/21/4/045008)

J. Micromech. Microeng. **21** (2011) 045008 (10pp) doi:10.1088/0960-1317/21/4/045008

An adaptive feedback circuit for MEMS resonators

Xiao Zhu Fan, Nathan Siwak and Reza Ghodssi

Electrical and Computer Engineering Department, Institute for System Research, University of Maryland, College Park, MD 20742, USA

E-mail: xiaozfan@umd.edu, npsiwak@umd.edu and ghodssi@umd.edu

Received 4 January 2011, in final form 26 January 2011
Published 1 March 2011
Online at stacks.iop.org/JMM/21/045008

Abstract

The first adaptive feedback circuit capable of detecting resonant frequencies for a wide range of MEMS resonators is presented. The feedback system presented implements a hill-climbing algorithm that sweeps actuation frequencies, locking onto the resonance condition at maximum cantilever amplitude response without limitations on the frequency range. To demonstrate its adaptability, a circuit implementation of this feedback algorithm was used to detect the resonant frequency of eight different cantilever-based sensors (width (W) = 1.4 μm, length (L) = 40–75 μm, and thickness (T) = 1.8 μm), resonating at 201.0 to 592.1 kHz. Additionally, the same circuit was used to track resonant frequency shifts due to isopropanol adsorption on three different chemical sensors with no modifications. The feedback electronics integrated with these resonator sensors provide a mass resolution limit of 123 femptograms. The realization of this system will enable real-time chip-scale sensor systems, providing an alternative to external instrumentation modules that perform sensor control and monitoring.

(Some figures in this article are in colour only in the electronic version)

1. Introduction

The compatibility of size and fabrication processes between micro electromechanical systems (MEMS) and microelectronic circuits has enabled the efficient system integration of both technologies. While low-power MEMS sensors allow for simple devices with smaller footprints and high functionality, circuit elements provide device control and electrical readout [1]. Taking advantage of both technologies can enable a variety of promising hybrid systems. A large portion of today's MEMS devices consist of resonators due to their wide range of applications, including oscillators [2], RF MEMS [3], and chemical and biological sensors [4]. As a result, circuit designers have developed CMOS circuitry for integration with microresonators, most often to achieve monolithic systems without the reliance on external instruments or components, enabling the entire system to be miniaturized, portable, and autonomous [5]. CMOS circuits have been shown to enhance systems by increasing resonator displacement readout resolution [6], enhancing the quality (Q) factor of resonators [7, 8], compensating for parasitic capacitive effects [5], and selecting vibration modes [9]. Detecting the natural frequency of a resonator is the primary role of these circuits, performing timing functions, driving the resonator, and sensing analytes [10, 11]. In addition, circuit integration can provide the real-time measurement of the resonator, which enables the development of feedback systems [12, 13] and enhances the functionality of the system through device sensitivity enhancements [14] and autonomous resonant frequency (f_o) tracking [15].

Self-excitation circuits are common feedback circuits that utilize displacement signals to autonomously drive microresonators at their resonant frequency by adjusting the actuation signal's gain and phase. A frequency counter is then connected to detect and track its resonant frequency with resonant frequency resolution detected down to 1 Hz (f_o = 5475 Hz) [16]. The gain and phase compensation stages require each circuit to be tailored to an individual device, reducing the possibility of a universal readout and feedback circuit. The requirement for a frequency counter also limits the application of the system. Another popular circuitry used is the phase lock loop (PLL) to lock onto the resonant frequency of the resonator by locking a voltage-controlled oscillator (VCO) to the phase of the input reference signal. The VCO can provide a direct readout of the resonant frequency and offers high-frequency stability ($f_{\min}$ = 1 Hz, f_o = 3 MHz [17]).

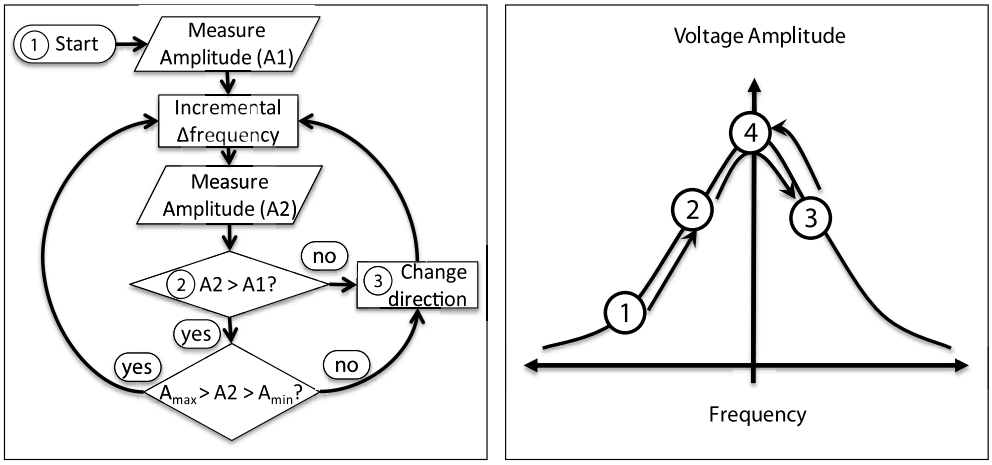

Figure 1. Diagram describing the hill-climbing optimization algorithm used to locate the maximum amplitude at the resonant frequency.

Table 1. Limitation of feedback loops for the detection and tracking of resonant frequency.

	Resonant frequency range	Resonant frequency shift range	Resonant frequency shift step	Readout
Self-excitation	Phase compensation	Phase compensation	Phase compensation	Freq. counter
Phase lock loop	Pull-in range, VCO output	Hold range, VCO output	Pull-out range, VCO output	Direct
Hill climbing	VCO output	VCO output	VCO output	Direct

However, it suffers from limited detectable resonant frequency and resonant frequency shift (Δf_o) ranges. Table 1 summarizes the limitations of feedback approaches.

The sensitivity and limitations of each feedback circuit are dependent on each individual circuit design used. The phase compensation stage of the self-excitation circuit and the pull-in and hold ranges of the PLL are tailor designed for their respective system and application. The inherent limitations of the pull-in, pull-out, and hold ranges of the PLL arise from the oscillator locking onto the phase of the reference signal. The ranges of the PLL are dependent on the gain and filters of the PLL, which depend on their respective system design.

The feedback system presented here adapts to a wide range of resonators by implementing a hill-climbing algorithm, which drives the cantilever at its maximum amplitude response and finds this through a frequency sweep. The inherent limitations of the feedback circuit to locate resonant frequency and frequency shift range are eliminated due to the omission of a phase relationship. The practical limitation of the system is solely restricted by the performance of the VCO.

Here, the feedback circuit has been implemented with a previously reported indium phosphide (InP) resonator sensor [18] as a platform to investigate the adaptability of the circuit by detecting a wide range of cantilever resonant frequencies. In addition, to verify the tracking of resonant frequency shifts with respect to time, a mass shift was induced by adsorption of chemical molecules onto the surface of the cantilever. Although the system is not optimized for chemical vapor sensing, the feedback algorithm is used to demonstrate the feasibility for such an application.

This paper is organized as follows. In section 2, the feedback circuit, circuit implementation, PSPICE simulation, and resonator design of the system are detailed. Sections 3–5 are divided into resonator and sensor characterization subsections, describing the testing setup, testing results, and discussion of these two experiments. The last section provides the conclusions.

2. Design

2.1. Hill-climbing algorithm

A hill-climbing algorithm is an optimization technique that is used to locate the local extrema of a system. This algorithm is generally used in computation and search algorithms [19, 20], specifically cost minimization [21], real-world modeling [22], and artificial intelligence [23]. Optimization algorithms are seldom used in the field of MEMS for device operation, with most examples in design parameter optimization [24] and device calibration [25].

The optimization technique is implemented in this design to locate the local maximum amplitude of the resonator system, through which the resonant frequency can be determined. Hill climbing maximizes (or minimizes) a function by locally sweeping the value of the function, comparing the present state to the past state until an extremum is located. If the present state is preferred over the past state, the direction of the local sweep remains the same. However, if the past state is preferred, the direction of the sweep reverses (see figure 1). More advanced optimization algorithms are available that perform a similar function; however, due to the simplicity of the resonator frequency response, this algorithm is well suited for this application.

The hill-climbing algorithm sweeps a range of actuation frequencies starting at a random point in a random direction. The algorithm will continue to sweep the frequency in the more

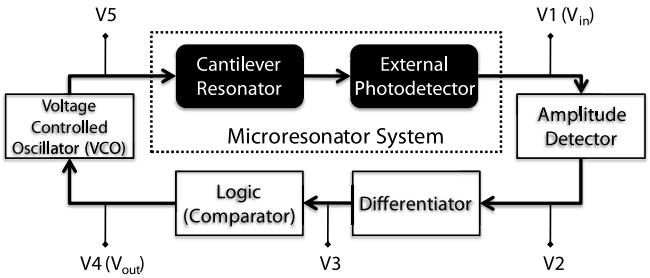

Figure 2. Feedback circuit diagram showing a four-stage circuit integrated with a chemical resonator sensor.

favorable direction until a maximum response is achieved at the resonant frequency, f_o. Once f_o is reached, a small steady-state oscillation will occur as the algorithm sweeps around the optimal point, changing directions as it passes the apex. The small steady-state oscillation around the resonant frequency is averaged (using a running average) to determine an estimate of the resonant frequency based on the assumption that the averaged time period is much smaller than the time required to shift the resonant frequency.

2.2. Feedback circuit implementation

The hill-climbing algorithm is implemented using a four-stage mixed-signal feedback circuit, consisting of an amplitude detector, a differentiator, logic control, and a VCO stage, each of which will be further detailed in subsequent subsections. The resonator displacement signal is fed into the amplitude detector stage as the input of the feedback circuit. Completing the feedback is the VCO output that drives the resonator at a controlled actuation frequency (see figure 2). The output signal to the system is taken from the VCO input bias voltage, which is correlated to the resonator driving frequency. At the steady state, the drive frequency will oscillate around the resonant frequency. The voltages in between each stage are labeled and they will be referred to as $V1$ through $V5$ in the later sections.

2.2.1. Amplitude detector stage. The amplitude detector stage is composed of a high-pass filter, an amplifier, a precision full-wave rectifier, and a low-pass filter. The displacement input signal, $V1$, of the resonator systems in question ranges from 100 kHz to 1 MHz in frequency and exhibits millivolt amplitude, with a constant dc offset. To obtain the amplitude of the oscillating signal, $V1$ is first passed through a high-pass filter and amplified ($G = 100$ V/V). The signal is rectified using a precision full-wave rectifier, which consists of summing two precision half-wave rectifiers, one of which is inverted and the amplitude doubled.

The precision rectifier is designed using generic components consisting of two high-speed, low-noise op-amps and diodes. The amplitude of $V1$ is obtained by capturing the envelope of the rectified signal using a simple RC low-pass filter.

2.2.2. Differentiator stage. The differentiator stage, which is composed of low-pass filters and a differentiator, determines the change in resonator signal with respect to time. A favorable and an unfavorable change in response are defined as a positive and negative differentiation signal, respectively. The differentiation stage will cause an intrinsic gain in the frequency signal. Any high-frequency ripple, resulting from the previous envelope-detecting stage, will be amplified by orders of magnitude, drowning out any useful differential signal. Therefore, low-pass filters are applied to $V2$ to further reduce ripple and to maintain an acceptable signal-to-noise (S/N) ratio.

2.2.3. Logic stage. The logic stage determines the direction of sweep based on the change in response with respect to time, $V3$. This stage will trigger a change in direction when the differentiation signal changes from positive to negative, but maintain its direction for all other circumstances. This stage is comprised of a Schmitt trigger, a toggle flip flop (T-FF), and an integrator. A Schmitt trigger is a comparator with positive feedback that has a tunable threshold ($V_T = \pm(R_1/R_2)V_S$) that $V3$ must achieve before the output is triggered. Utilizing the Schmitt trigger provides greater noise immunity compared to that of a regular comparator, which would cause rapid switching between high and low states due to signal noise.

The direction of the frequency sweep is based on the direction of signal change as determined by a T-FF, which changes state when the T input is held high and the clocked input is strobed, described by the characteristic equation

$$Q_{\text{next}} = T \oplus Q. \tag{1}$$

If T is held high and the T-FF toggles on positive edge clock, the output toggles when the clock goes from low to high. When the Schmitt trigger output is connected to the T-FF clock and low and high states correspond to negative and positive differential signal, the T-FF output will toggle when the signal response switches from positive to negative. Conversely, a change from a negative to a positive signal results in the output state remaining unchanged. The output state of the T-FF determines the direction of the driving frequency sweep (high and low correspond to increase and decrease in driving frequency, respectively). An integrator is attached in series with the T-FF to integrate the digital signal, generating an input voltage bias, $V4$, serving as the VCO input and an output of the resonator feedback system.

2.2.4. VCO stage. The VCO stage is the driving stage of the resonator feedback system. The VCO output, $V5$, is an oscillating signal whose frequency is dependent on the input voltage bias, $V4$. The output waveform is a square wave from 0 to 5 V, whose output frequency range can be tuned with biasing resistors and capacitors. Further signal processing can be performed on $V5$ following the VCO output if required for driving the resonator, such as signal amplification.

By sweeping $V4$, the frequency response of any resonator in the tuned range can be obtained. If the VCO is oscillating around the resonator's maximum response at f_o, the resonant frequency can be inferred by monitoring the VCO's mean input bias, as described above.

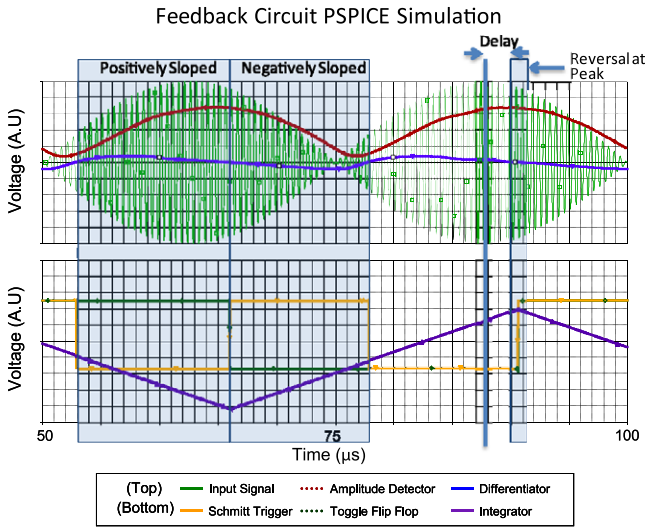

Figure 3. Circuit schematic of the logic stage comprising a Schmitt trigger, a T-FF wired from a J-K FF, and an RC integrator.

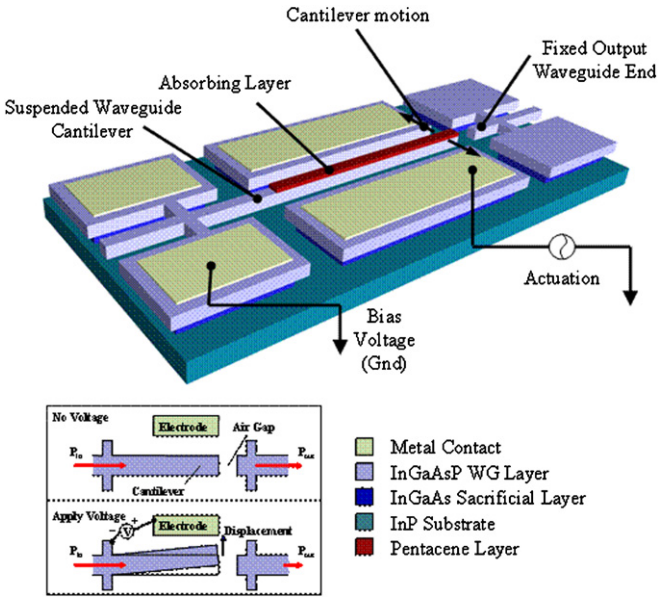

Figure 4. Three-dimensional schematic of the cantilever waveguide resonator and illustration of the readout operational principle [18] (© 2009 IEEE).

2.3. PSPICE simulation

An open-loop circuit was designed and simulated in Cadence PSPICE to verify the implementation of the hill-climbing algorithm, determine the delay and frequency response of the circuit, and measure the acceptable noise level of each stage. A resonator response, *V*1, used as the input signal to the feedback circuit, was simulated using an amplitude-modulated signal with a message frequency and a carrier frequency of 2 MHz and 20 kHz, respectively, with an amplitude of 50 mV. Initial simulation results showed high noise levels, signal distortion, and high current draw. Active low-pass filters were added after the amplitude detection stage to eliminate the ripple noise, which gets amplified by the differentiation stage. The V_T of the Schmitt trigger was raised to reduce the impact of signal noise but, as a result, it caused a delay in signal propagation due to the extended time required to achieve the threshold level.

The final simulation results, shown in figure 3, demonstrate the successful implementation of the open-loop circuit, showing the output at each stage. The expected operation of each stage was investigated. The simulation output, at *V*4, switched the sweeping direction when the amplitude changed from increasing to decreasing, but retained the direction of sweep when the amplitude changed from decreasing to increasing. A delay time of 10 μs was calculated between *V*1 and *V*4. These μs delay times are acceptable for the designed application of resonator characterization and chemical vapor sensing, but should be minimized as much as possible to decrease oscillation amplitude around f_o. This issue will be further discussed in the following sections.

2.4. Resonator design

The device that is used for testing this feedback circuit is an electrostatically driven in-plane InP cantilever resonator. Many different methodologies have been developed to sense analytes using microcantilevers each with their own advantages and disadvantages. Measuring the induced resonant frequency shift caused by mass loading on the resonator is one of the more commonly used methods to measure the cantilevers [4], and this will be used in this work to characterize the tracking ability of the feedback circuit on a previously implemented system.

The readout scheme used for the cantilever sensor here is based upon the change of optical coupling between a misaligned air-cladded cantilever waveguide and a fixed output waveguide. A diagram showing the cantilever waveguide sensor components and an illustration of the readout concept is shown in figure 4.

Optical power is coupled onto chip and passed through the waveguides. By applying voltage between the cantilever and a parallel actuation electrode, the cantilever is displaced in-plane due to electrostatic force. This displacement changes the amount of optical power that is coupled into the output waveguide from the cantilever input waveguide. The displacement of the cantilever is determined by measuring the output optical power from a photodetector, whose output signal is used as the input signal to the feedback circuit. The ultimate sensitivity of the displacement is dependent on the sensitivity of the photodetector, coupling efficiency across the coupling air gap, and the optical loss in the waveguide.

The resonator system used here is fabricated in a III–V semiconductor, providing for the monolithic integration of multiple electro-optical components. In this case, the direct bandgap semiconductor InP is used, allowing the integration of optical sources, waveguides, and photodetectors within the same substrate. Motivated by such an application, InP cantilevers such as those used in this work have been previously investigated [16]. The knowledge acquired from previous demonstrations allows for independent verification of the results obtained from the feedback circuit and helps to

validate its effectiveness. A more detailed description of the waveguide cantilever platform was previously reported in [16].

The approximate resonant frequency of the cantilevers can be expressed as

$$f_o = \frac{1}{2\pi}\sqrt{\frac{3EI}{L^3 c_o m_o}}, \tag{2}$$

where E is Young's modulus, I is the cantilever area moment of inertia, L is the cantilever length, m_o is the cantilever mass, and $c_o = 0.24$ is a mass correction factor for a rectangular beam. To include the added mass of the analyte to the cantilever, equation (3) is modified by including m_A and c_A, absorbed mass and a constant that describes the position of the added mass ($0.24 < c_A < 1$, where $1 =$ concentrated at the cantilever tip and $0.24 =$ spread over the entire cantilever surface). By increasing the mass on the cantilever, f_o decreases. By monitoring the change in resonant frequency, Δf, the change in mass, Δm, is therefore determined,

$$f_o = \frac{1}{2\pi}\sqrt{\frac{3EI}{L^3(c_A m_A + c_o m_o)}}. \tag{3}$$

The mass loading sensitivity can be expressed as the ratio of the measured frequency shift to the mass change [4],

$$\frac{\Delta f_{\min}}{\Delta m_{\min o}} = \frac{f_o c_A}{0.48 \cdot m_o}. \tag{4}$$

Equation (3) shows that decreasing L will increase its f_o, and thus increase the sensitivity of the device, as defined in equation (4). The beam is electrostatically driven by an electrode that is positioned in parallel. The required voltage to deflect the cantilever can be derived by calculating the voltage difference necessary to appreciably actuate the cantilever, assuming small displacement with respect to the actuation gap,

$$V = \sqrt{\left(\frac{2g^2}{\varepsilon_o t}\right)\left(\frac{Ewt^3}{4L^3}\right)\delta}. \tag{5}$$

V is the applied dc voltage between the electrode and the cantilever, t is the cantilever thickness, w is the cantilever width, L is the cantilever length, δ is the cantilever end deflection, ε_o is the permittivity of free space, and g is the actuation gap of the cantilever. The required actuation voltage increases with a decrease in L, which will be a limiting factor when deciding the range of resonator devices to test. The required actuation voltage is also limited by the minimum detectable δ, which is dependent on the sensitivity of the photodetector.

2.5. Sensing mechanisms

A simplified sensing approach was selected to verify the proof of concept of the tracking ability of the feedback circuit. Without a receptor layer, adsorption is the mechanism that is observed for non-selective molecule attachment to the surface of the resonator. Adsorption is the adhesion of adsorbate (molecules of gas, liquid, or dissolved solids) to the adsorbent surface due to surface energy. The atoms at the surface, not wholly surrounded by other adsorbent atoms, have exposed binding sites and therefore can attract molecules in its surrounding environment. The mechanism of the bond is species dependent, but can be generally classified as physisorption or chisorption, characteristic of weak van der Waals forces or covalent bonding, respectively.

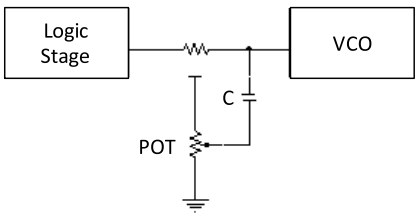

Figure 5. Circuit schematic showing the integrator capacitor and the potentiometer wiring configuration, where C and POT controlled the transient and steady-state operation, respectively.

Table 2. Electrical components used.

Component	Value
Op Amp	LM318
Diode	D1N914
Toggle flip flop	CD74HCT109E
Inverters	SN74LS04N
VCO	CD74HC7046AE
VCO R_{Bias}	152 kΩ
VCO C_{Bias}	50 pF

3. Testing setup

3.1. Circuit construction

The feedback circuit was built using discrete IC components on a circuit board, powered by ±12 V analog and 5 V digital rails. The resonators used had widths and thicknesses of 1.4 and 1.8 μm, respectively, with lengths ranging from 45 to 75 μm. Based on equation (2), expected resonant frequencies should range from 2.8 to 63.6 kHz for these device lengths, respectively. The biased VCO has a resolution of 4.4 mV kHz^{-1} from 198 to 971.3 kHz with 1.1–4.5 V input and R_{Bias} and C_{Bias} of 152 kΩ and 50 pF, respectively. A complete list of the electrical components used can be found in table 2.

3.2. Resonator characterization utilizing detection of resonant frequency

During testing, 10 min datasets were taken. Acquisition of VCO input bias and photodetector coupling strength was recorded using a LabVIEW program with a sampling frequency of 2 kHz. An open-loop system was first tested to obtain the frequency response of the resonator under test. The open-loop setup (Logic and VCO stages disconnected, see figure 2) consisted of a function generator voltage sweep connected to the VCO input bias ($V4$) to facilitate a frequency sweep of the actuation signal. The amplitude of the resonator response and the sweep direction was then obtained and verified at the $V2$ and logic stage outputs.

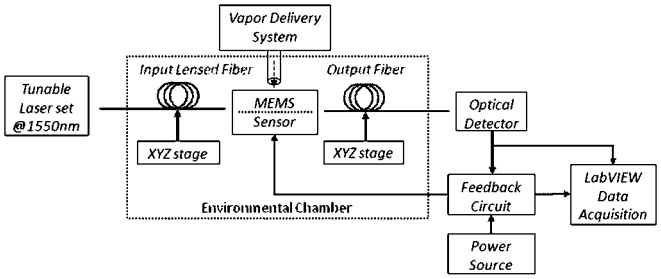

Figure 6. Block diagram showing the experimental setup.

The closed-loop circuit was then tested to automate the resonator measurement. The closed-loop system was completed by connecting the output signal of the logic stage to the input of the VCO, eliminating the simulated VCO input signal provided by the function generator. The initial VCO input bias was determined by the initial charge stored on the integrator capacitor in the previous stage, which was controlled by a potentiometer, as seen in figure 5. After the initial turn-on, the operation of the circuit was isolated to the small signal across the capacitor, meaning that any dc voltage set by the potentiometer did not influence the circuit operation. The transient and steady-state operation points are defined here as the operation period before and after the feedback system has locked onto the resonant frequency of the device, respectively.

3.3. Resonator sensing utilizing resonant frequency tracking

The feedback circuit was tested with a resonator in a vapor chamber to track the shift in cantilever resonant frequency caused by the added mass. The vapor chamber setup consisted of a fluid reservoir bubbler (50 mL glass filtering flask), which used nitrogen as a carrier gas to transport vaporized analyte from the fluid reservoir into an enclosed environmental chamber. The $20 \times 45 \times 50$ cm environmental chamber was fitted with electrical, optical, and gas feed-throughs, and contained within the sensor chip, two probes for electrical contacts, and two *xyz* positioners for optical input and output fiber alignment (see figure 6). For these experiments, isopropyl alcohol (IPA) vapor was chosen due to its high vapor pressure at room temperature, nontoxic nature, and immediate availability. IPA vapor was introduced to the chamber followed by ambient air for approximately 15 min cyclically. This was repeated multiple times for each device to demonstrate the repeatability and stability of the feedback circuit to track the shift in resonant frequency. Three sensors with different f_o were tested. The mass-induced frequency shift is assumed to be due to the surface adsorption of IPA. For this particular testing iteration, no receptor layer was used to simplify the device fabrication and establish an initial proof-of-concept of the feedback circuit's operation.

4. Results

4.1. Detection of resonant frequency

Open-loop design resulted in a clear peak at f_o at the output of the amplitude detection stage when the function generator was used to sweep the actuation frequency at the rate of 1 Hz. The open-loop frequency scan of deviceA ($W = 1.4\ \mu$m, $L = 55\ \mu$m, $T = 1.8\ \mu$m) showed a maximum amplitude at 314 kHz, which was estimated to be its resonant frequency. High noise levels causing greater circuit instability were an initial concern during testing. To combat this, the threshold level of the Schmitt trigger was increased to provide improved noise immunity. An increased delay of 30 ms was observed at the output of the logic stage due to the adjusted threshold level. This open-loop integration of the feedback system with the resonator cantilever demonstrated that it was feasible to locate the resonant frequency by using the circuit components as designed; however, to autonomously locate and track the resonant frequency of the resonator, closed-loop feedback was required.

The closed-loop feedback began with the transient stage frequency sweep, exhibiting a typical RC time constant as the integrator capacitor charged and discharged. The direction of the sweep, charging or discharging of the capacitor, was random since the initial state of the T-FF was random. If the direction of the initial sweep failed to locate a peak in response, the integrator would hit a voltage rail until the T-FF was toggled to change the direction of the sweep. Presently, this was achieved by adjusting a potentiometer controlling the Schmitt trigger threshold level. However, an additional comparator can be added to compare the integrator with the rail to automate this toggling. As the resonant frequency peak was approached, the amplitude detector signal increased, creating a positive differential signal. The change from a positive to negative differential signal marked the apex of the peak. A decrease in amplitude triggered the Schmitt trigger as it surpassed V_T, toggling the VCO to be swept back toward the apex, f_o. Operating in steady state, the feedback circuit oscillated around f_o, the apex of the resonant frequency peak. The direction of sweep continuously oscillates toward the direction of f_o, and as a result the signal is considered locked onto the resonant frequency. An example of the output signals during locked operation can be seen in figure 7.

DeviceA ($W = 1.4\ \mu$m, $L = 55\ \mu$m, $T = 1.8\ \mu$m) exhibited a mean input VCO bias of 1.721 V, which corresponded to a frequency of 314.0 kHz, a percent error of 1.54% compared to its calculated resonant frequency of 309.3 kHz. The oscillation frequency around f_o was approximately 800 Hz with an amplitude of 21 mV, which is controlled by the Schmitt trigger threshold setting. The standard deviation of the input VCO bias' running average was 0.16 mV, corresponding to a frequency of 29.7 Hz.

Six devices ranging in length from 40 to 75 μm ($W = 1.4\ \mu$m, $T = 1.8\ \mu$m) were tested with the same feedback circuit, resulting in the measurement of their resonant frequencies ranging from 592 to 201 kHz, respectively (see figure 8). The minimum time averaged standard deviation of the set was 11.8 Hz for DeviceB ($W = 1.4\ \mu$m, $L = 75\ \mu$m, $T = 1.8\ \mu$m). Based on this minimum detectable frequency shift, the mass sensitivity of the system, defined by equation (4), is 123 fg. The maximum time averaged standard deviation of these devices was 362 Hz.

The resonant frequency of these resonators was successfully and repeatedly locked onto using the designed

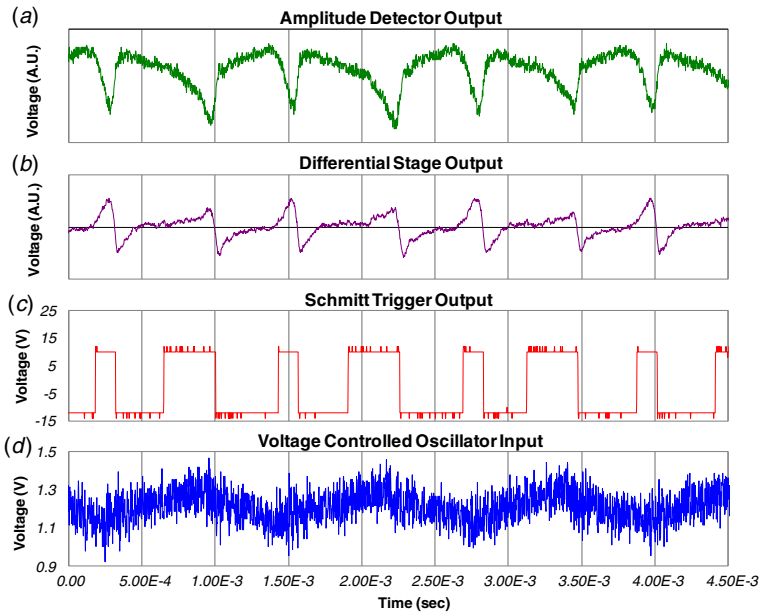

Figure 7. Output of individual stages of the feedback circuit while locked on to the resonant frequency. (*a*) Output of the amplitude detector showing a periodic peak amplitude, (*b*) differential signal of the amplitude detector, (*c*) Schmitt trigger output detecting the direction of the slope and (*d*) input of the VCO showing oscillation around a bias voltage.

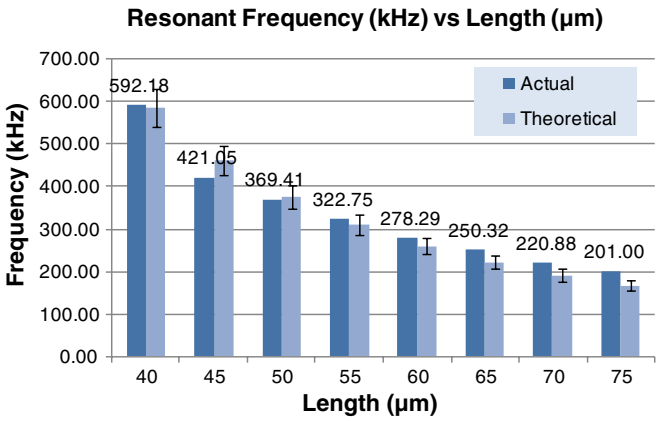

Figure 8. Resonant frequency detection of cantilevers ranging from $L = 40$ to 75 μm together with their theoretical resonant frequency. Error bar for the theoretical values is based on 0.1 μm fabrication tolerance.

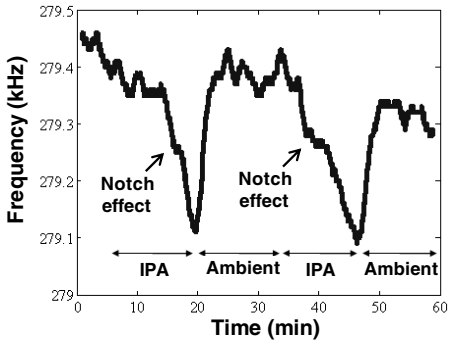

Figure 9. Resonant frequency shift due to IPA adsorption on the cantilever surface measured using the feedback circuit. The device tested ($W = 1.4$ μm $L = 60$ μm) shows a repeatable shift of ~250 Hz.

feedback circuit. The estimated resonant frequencies of multiple 10 min trial runs were all within the stated standard deviation. Datasets of up to 60 min long were obtained with no signs of failure or deviation from the 10 min scans. During the scans, there were occasions when the circuit lost track of the resonant frequency, requiring the circuit to find and lock onto f_o again. The time required to relocate f_o appeared to be based upon the time required to toggle the T-FF to reverse the sweep direction, normally less than a millisecond.

Device lengths outside the 40–75 μm range were tested. However, steady-state operation was not consistently achieved for these devices and is discussed in this section.

4.2. *Resonant frequency tracking*

Dynamic resonant frequency shift measurements were conducted with three resonators of length 55, 60, and 65 μm. The closed-loop circuit was used to track shifts of 330, 250, and 390 Hz from the three resonators, corresponding to the mass changes of 1.37, 1.34, and 2.67 pg, respectively. Mass loading was assumed to be due to the surface adsorption of IPA vapor onto InP cantilever surface because f_o shifts due to secondary effects, such as squeeze film dampening and change in the refractive index of the air inside the chamber, were calculated to be below the resolution of the current circuit implementation and deemed insignificant. The introduction of ambient air allowed for the desorption of the IPA due to the change in IPA vapor concentration in the environmental chamber. As shown in figure 9, the resonant frequency returned to its natural frequency in ambient air after each introduction of IPA vapor.

A notch was observed midway through the IPA introduction stage. This notch was present during each of the periods of IPA introduction and all three sensor-testing traces. A drift in f_o was seen during the 60 min experiment; this effect was observed in previous chemical sensing experiments conducted with the same sensing setup utilizing a different measurement technique.

The tracking of resonant frequency for each device was achieved without any modifications to the circuit, further demonstrating the adaptability of this approach by functioning with multiple devices. The sensitivity of this sensor system is calculated to be 120 fg based on the standard deviation of the noise level of the steady-state signal. Utilizing a receptor layer on the resonator will greatly benefit the sensor system by increasing its sensitivity and selectivity.

5. Discussion

5.1. Detection of resonant frequency

Theoretically, with ideal resonators and circuit optimization, the implementation of the hill-climbing algorithm is capable of detecting the resonant frequency of any device. However, due to limitations of this resonator design, noise interference in the system, and frequency response of the IC components, this feedback system was limited to a subset of devices. The upper bound to the device length of 75 μm was due to the limited optical coupling through the device. Longer cantilevers exhibited a greater out-of-plane curvature due to film stress, causing loss in optical coupling and resulting in a very poor S/N ratio, preventing the circuit from establishing a consistent steady-state frequency lock.

The lower bound to the device length range was limited by the voltage limits and frequency responses of electronic components. As the length of cantilever decreased, the cantilever f_o increased and the required actuation voltage increased due to increased device stiffness (see equation (5)). In order to boost the VCO's 5 V output voltage, an amplifier is needed. The available amplifiers do not posses high enough bandwidth to operate in the MHz frequency ranges. As the driving frequency approached MHz, the signal was also distorted through the various stages of the feedback circuit, limiting the operation to lower frequency devices. This effect is not inherent to the algorithm but is directly related to the resonator and circuit components and construction.

Resonant frequencies detected using the feedback circuit agreed with theoretical calculations within error and were independently verified using other methods as detailed in [10]. The measured and theoretical resonant frequency discrepancies can be attributed to fabrication imperfections. The detection resolution of 11.8 Hz is of the same order of magnitude as that of a ring down testing scheme using external instrumentation previously used on the system.

The amplitude of the oscillating signal around f_o was consistent during the 10 min baseline measurement for the majority of the experiments. However, some tests showed a change in the amplitude of oscillation, which was attributed to a drift in optical coupling in the resonator setup. A mechanical drift in optical fiber alignment can cause a decrease in optical coupling leading to a decrease in displacement signal strength. The weaker signal causes an increase in time required to surpass the V_T of the Schmitt trigger, which resulted in the larger amplitude of oscillation around f_o. This effect was observed in the testing of DeviceC ($W = 1.4$ μm, $L = 65$ μm, $T = 1.8$ μm), where an approximate 5 mV increase in amplitude corresponded to a drift in coupling of 9%. If the resonator setup can eliminate this drift and increase the displacement signal SNR, the standard deviation of the feedback system output could be minimized further and thus increase the overall sensitivity. A solution would be to implement an integrated on-chip optical source and detector to increase coupling efficiency and eliminate the drift in optical coupling caused by the external setup.

Another limitation observed during testing was the failure of the feedback loop to lock onto the f_o of a resonator that exhibited two resonant frequency peaks that were within 100 kHz of each other. DeviceD ($W = 1.4$ μm, $L = 60$ μm, $T = 1.8$ μm) was used as test device and had two superimposed resonant frequencies, 224.2 and 329.0 kHz. The two resonant frequency peaks were a result of the lateral as well as an out-of-plane actuation. Due to the rectangular cross-section for the beams, the cantilever's in-plane resonant frequency was 81.9 kHz lower than its out of plane resonant frequency. The feedback circuit experienced difficulty locking on to one peak due to the delay, caused by the elevated trigger threshold, enabling the circuit to reach the second peak before it had a chance to toggle and return to the first peak. As a result, the hill-climbing algorithm failed to consistently lock to a single peak when the circuit did not respond to the trough due to their overlap. This problem could be solved by reducing the V_T of the Schmitt trigger, and thus the delay, enabling a faster toggle after the peak, before entering the trough. This limitation was not overcome in this work because the reduced V_T required a higher SNR than what was obtainable with the used setup.

5.2. Resonant frequency tracking

The versatility and the dynamic tracking ability of the feedback circuit were demonstrated by the autonomous detection of IPA vapor using three different resonator devices. The typical time constant of vapor adsorption, of the order of minutes, as shown here, is much greater than the millisecond delay observed in the simulation and open-loop testing, and allowed us to be confident in the assumptions made. The notch and drifting effects have been determined to be associated with the sensor testing setup rather than the tracking circuit itself.

The notch behavior is believed to be caused by the condensation mechanics of IPA molecules on the surface of the cantilever since the notch consistently appears $\sim$5 min after introduction of IPA vapor for each resonator tested. Because of the mechanism of addition of mass due to adsorption, not the often-used absorption, the physical attachment of gas molecules on a solid surface is different from that of an expected simple exponential decay observed from absorption-based sensors or porous solid substrates. When taken

into consideration, multilayer adsorption, BET isotherm [26] predicts that the amount of adsorption increases indefinitely as the pressure is increased since there is no limit to the amount of condensation. The degree of the notch is dependent on the relative strengths of adsorption to the surface and condensation of the pure adsorbate.

The f_o drifting effect is attributed to long-term changing ambient room conditions also observed previously in [5]. This feature can be minimized by establishing a more stable environment with humidity and temperature control.

The origin of the noise experienced in the final output voltage is difficult to determine because of the contribution from a wide range of possible sources. The change in environmental conditions inside the chamber between nitrogen and ambient conditions may have caused a drift in the electrostrictive *xyz* stages, changing the optical coupling onto and out of the chip. Mechanical vibrations may have caused electrical spikes and discontinuities in the system, causing the algorithm to lose track of the peak temporarily. The calculated sensitivity of 120 fg utilizing the feedback circuit is of the same order as the calculated sensitivity previously reported [16] of this sensor system. As a result, the noise may be associated with the intrinsic noise in the sensor readout technique since the system has not been fully optimized with integrated components.

6. Conclusion

A hill-climbing optimization algorithm was implemented in a mixed-signal feedback circuit to detect the resonant frequency of a resonant cantilever for the first time. The circuit was designed, simulated, and constructed to detect the resonant frequency of resonators. Due to the versatility of the hill-climbing algorithm, the resonant frequency detection circuit did not need to be tailored for individual resonators as is the case with other detection methodologies. The resonant frequency of a wide range of cantilevers and the mass-induced resonant frequency shift of three resonators have also been reported using this single unmodified feedback circuit, demonstrating its adaptability and potential as universal control circuit.

The adaptability and precision of the feedback circuit to detect the f_o of resonators are ultimately limited by the individual IC characteristics, such as the output frequency range of the VCO and the bandwidth of the op-amps used. The sensitivity of the system is dependent on the noise levels present, which includes the electrical noise of the circuit and the intrinsic noise of the resonator sensors. The integration of this universal feedback circuit with resonator devices allows for more flexible real-time readout and enables the development of smart chip-scale microsystems. This circuit can also be applied to other applications that have a peak-like response, such as 3D MEMS fiber aligners [27], tunable lasers [28], and optical filters [29].

Acknowledgment

This work was supported in part by the National Science Foundation.

References

[1] Suleski T J and Kolste R D T 2005 Fabrication trends for free-space microoptics *J. Light. Technol.* **23** 633
[2] Otis B P and Rabaey J M 2002 A 300 umW 1.9 GHz CMOS oscillator utilizing micromachined resonators *Proc. 28th European Solid-State Circuits Conf. (24–26 September 2002)* pp 151–4
[3] Yao J J 2000 RF MEMS from a device perspective *J. Micromech. Microeng.* **10** R9–38
[4] Lavrik N V, Sepaniak M J and Datskosa P G 2004 Cantilever transducers as a platform for chemical and biological sensors *Rev. Sci. Instrum.* **75** 2229–53
[5] Baltes H, Brand O, Hierlemann A, Lange D and Hagleitner C 2002 CMOS MEMS—present and future *Proc. 15th IEEE Int. Conf. on Micro Electro Mechanical Systems (Las Vegas, NV, 2002)* pp 459–66
[6] Lee Y, Lim G and Moon W 2006 A self-excited micro cantilever biosensor actuated by PZT using the mass micro balancing technique *Sensors Actuators* A **130–131** 105–10
[7] Tamayo J, Humphris A, Owen R and Miles M 2001 High-*Q* dynamic force microscopy in liquid and its application to living cells *Biophys. J.* **81** 526–37
[8] Tamayo J 2005 Study of the noise of micromechanical oscillators under quality factor enhancement via driving force control *J. Appl. Phys.* **97** 044903
[9] Blokhina E, Pons J, Ricart J, Feely O and Pumar M D 2010 Control of MEMS vibration modes with pulsed digital oscillators: part I. Theory *IEEE Trans. Circuits Syst.* I **57** 1865–78
[10] Li Y, Vancura C, Kirstein K-U, Lichtenberg J and Hierlenmann A 2008 Monolithic resonant-cantilever-based CMOS microsystem for biochemical sensing *IEEE Trans. Circuits Syst.* I **55** 2551–60
[11] Acramone J, Misischi B, Serra-Graells F, Boogaart M, Brugger J, Torres F, Abadal G, Barniol N and Perez-Murano F 2007 A compact and low-power CMOS circuit for fully integrated NEMS resonators *IEEE Trans. Circuits Syst.* II **54** 377–81
[12] Edvardsen A E, Aune A, Hok B and Yitterdal T A CMOS analog integrated circuit for actuation and readout of a MEMS CO_2 sensor *Proc. Norchip Conf. (8–9 November 2004)* pp 28–31
[13] Bedair S S and Fedder G K 2004 CMOS MEMS oscillator for gas chemical detection *Proc. IEEE Sensors (24–27 October 2004)* pp 955–8
[14] Li Y, Vancura C, Hagleitner C, Lichtenberg J, Brand O and Baltes H 2003 Very high *Q*-factor in water achieved by monolithic, resonant cantilever sensor with fully integrated feedback *Proc. IEEE Sensors Conf. (22–24 October 2003)* vol 2 pp 809–13
[15] Vancura C, Li Y, Kirstein K, Josse F, Hierlemann A and Lichtenberg J 2005 Fully integrated CMOS resonant cantilever sensor for bio-chemical detection in liquid environments *Proc. 13th Int. Conf. on Solid-State Sensors, Actuators and Microsystems (Seoul, Korea, 5–9 June 2005)* vol 1 pp 640–3
[16] Ferrari V, Marioli D, Taroni A, Ranucci E and Ferruti P 1996 Development and application of mass sensors based on flexural resonances in alumina beams *IEEE Trans. Ultrason. Ferroelectr. Freq. Control* **43** 601–8
[17] Ferrari V, Marioli D and Taroni A 1996 Thick-film resonant piezo-layers as new gravimetric sensors *Meas. Sci. Technol.* **8** 42–8
[18] Siwak N, Fan X Z, Hines D, Kanakaraju S, Goldsman N and Ghodssi R 2009 Indium phosphide MEMS cantilever resonator sensors utilizing a pentacene absorption layer *J. Microelectromech. Syst.* **18** 103–10

[19] Xi B, Liu Z, Raghavachari M, Xia C H and Zhang L 2004 A smart hill-climbing algorithm for application server configuration *Proc. WWW (New York, 17–22 May 2004)* pp 287–96

[20] Zeng S, Shi H, Chen G, de Garis H, Kang L and Ding L Orthogonal dynamic hill-climbing algorithm for dynamic optimization problems *Proc. 2006 IEEE Congress on Evolutionary Computation (16–21 July 2006)* pp 1331–7

[21] Bunyaratavej P and Miller D 2002 An iterative hillclimbing algorithm for discrete optimization on images: application to joint encoding of image transform coefficients *IEEE Signal Process. Lett.* **9** 46–50

[22] Garey M and Johnson D S 1990 *Computers and Intractability: A Guide to the Theory of NP-Completeness* (New York: Freeman)

[23] Russel S and Norvig P 2002 *Artificial Intelligence: A Modern Approach* 2nd edn (Upper Saddle River, NJ: Prentice-Hall) pp 111–4

[24] Peters D, Bolte H, Marschner C, Nussen O and Laur R 2002 Enhanced optimization algorithms for the development of microsystems *Analog Integrated Circuits and Signal Processing* **32** 47–54

[25] Castillo J and Bifano T 2008 Adaptive optics calibration for a wide-field microscope *Proc. SPIE* **6888** 68880E

[26] Brunauer S, Emmett P H and Teller E 1938 Adsorption of gases in multimolecular layers *J. Am. Chem. Soc.* **60** 309–19

[27] Morgan B, McGee J and Ghodssi R 2007 Automated 2-axis optical fiber alignment using gray-scale technology *J. Microelectromech. Syst.* **16** 102–10

[28] Liu A Q, Zhang X M, Tang D Y and Lu C 2004 Tunable laser using micromachined grating with continuous wavelength tuning *Appl. Phys. Lett.* **85** 3684–6

[29] Datta M, Pruessner M W, Kelly D and Ghodssi R 2004 Design of MEMS-tunable novel monolithic optical filters in InP with horizontal Bragg mirrors *Solid-State Electron.* **48** 1959–63